Nanoscale

Accepted Manuscript

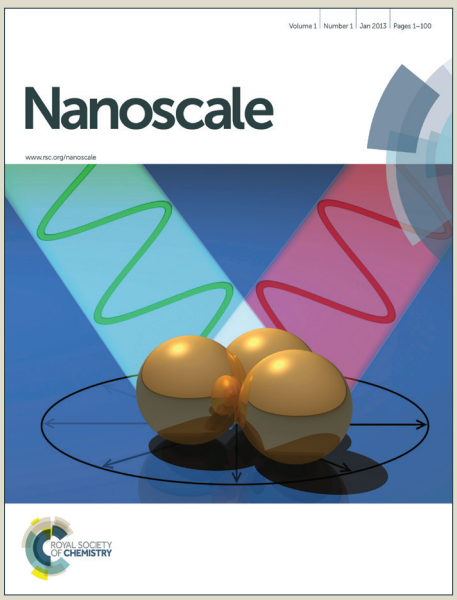

ROYAL SOCIETY OF CHEMISTRY

www.rsc.org/nanoscale

Nanoscale

RSCPublishing

ARTICLE

Fe/N/C hollow nanospheres by Fe(III)-dopamine complexation-assisted one-pot doping as nonprecious-metal electrocatalysts for oxygen reduction

Cite this: DOI: 10.1039/xoxxooooox

Received ooth September 2014,
Accepted ooth September 2014

DOI: 10.1039/xoxxooooox

www.rsc.org/

Dan Zhou,[a] Liping Yang,[b] Linghui Yu,[a] Junhua Kong,[a] Xiayin Yao,[a] Wanshuang Liu,[a] Zhichuan Xu,[a] and Xuehong Lu*[a]

In this work, a series of hollow carbon nanospheres simultaneously doped with N and Fe-containing species are prepared by Fe^{3+}-mediated polymerization of dopamine on SiO_2 nanospheres, carbonization and subsequent KOH etching of the SiO_2 template. The electrochemical properties of the hollow nanospheres as nonprecious-metal electrocatalysts for oxygen reduction reaction (ORR) are characterized. The results show that the hollow nanospheres with mesoporous N-doped carbon shells of ~10 nm thickness and well-dispersed Fe_3O_4 nanoparticles prepared by annealing at 750 °C (Fe/N/C HNSs-750) exhibits remarkable ORR catalytic activity comparable to that of commercial 20 wt% Pt/C catalyst, and high selectivity towards 4-electron reduction of O_2 to H_2O. Moreover, it displays better electrochemical durability and tolerance to methanol crossover effect in alkaline medium than the Pt/C. The excellent catalytic performance of Fe/N/C HNSs-750 towards ORR can be ascribed to their high specific surface area, mesoporous morphology, homogeneous distribution of abundant active sites, high content of pyridinic nitrogen, graphitic nitrogen and graphitic carbon, as well as the synergistic effect of nitrogen and iron species for catalyzing ORR.

1 Introduction

Fuel cells and metal-air batteries are promising electrochemical devices for energy storage/conversion. Owing to the sluggish kinetics of cathodic oxygen reduction reaction (ORR) in these devices, efficient ORR electrocatalysts are demanded for practical applications.[1] Carbon-supported Pt and/or its alloys have conventionally been employed as the cathode catalysts for ORR.[2] However, high cost, scarcity, methanol crossover effect and poor durability of the Pt-based catalysts hinder their large-scale applications. Hence, extensive efforts have been focused on developing metal-free or nonprecious-metal catalysts with high catalytic activity, low-cost and long-term stability.[3-7] A promising approach is to introduce nonprecious metals, such as Fe, Co or Mn, or their compounds into nitrogen-doped carbon materials, *e.g.,* N-doped carbon nanotubes, graphene and amorphous activated carbon,[3, 8-12] because N-doped carbon also exhibits good electrocatalytic activities towards ORR[13] and may work synergistically with the metal species, providing significantly improved catalyzing efficiency.[14-16]

For carbon-supported nonprecious metal species-nitrogen ORR catalysts, although the exact active sites and mechanism are still debatable,[16] it is generally believed that Fe-containing catalysts have higher ORR activity than those containing other nonprecious metals.[17] Besides the chemical compositions of the active sites, the morphologies of the catalysts are also important in determining their catalytic performances[15, 18, 19] because a large accessible surface area with pores of adequate size would allow more active sites be exposed to surrounding media and offer more efficient transport path for reactants and products.[20] Thus, it is essential to control both the morphology and structures of the catalysts.[21] A common approach to achieve both metal species-nitrogen active sites and favorable morphology for ORR catalysts is to incorporate metal species into/onto N-doped carbon nanostructures. For example, hollow carbon spheres[13, 22] with Co and Pt,[23, 24] and solid carbon nanospheres with Fe[25] have been prepared by utilizing polydopamine (PDA). PDA is a biomimetic adhesive polymer that can self-assemble to form spheres[25, 26] or form conformal coatings on various substrates and nanostructures,[22, 27, 28] and it is also an excellent carbon source that can yield thin carbon coatings with similar structures and electrical conductivities to that of N-doped multilayered graphene.[29-31] Metal salts could be easily adsorbed onto PDA surfaces or absorbed into PDA nanostructures, leading to metal-containing N-doped carbon nanostructures by carbonization. Using the aforementioned approaches, nitrogen- and metal-containing species are, however, incorporated in separate steps, *i.e.*, multi-step doping is involved. The preparation of hollow carbon nanostructures *via* one-pot simultaneous doping of N and metal-containing species has not been reported.

Recently, transition metal ion-mediated polymerization of dopamine has been reported, which enabled one-pot synthesis of transition metal ion-PDA complexes.[28] This opens up the possibility of simultaneously doping N and metal species into carbon nanomaterials. In this work, to simultaneously achieve desired chemical composition (*i.e.*, graphitic carbon effectively doped with both N and Fe species) and favorable morphology (*i.e.*, well-defined hollow cores and carbon shells as well as a large specific surface area with abundant mesopores) for ORR catalysts, hollow carbon nanospheres one-pot doped with both N and Fe-containing species were prepared for the first time by Fe^{3+}-mediated polymerization of dopamine on SiO_2 nanospheres, carbonization and subsequent KOH etching of the SiO_2 template. This facile and scalable method allowed us to eliminate multi-step doping process. Moreover, it allows high contents of Fe-containing species, and possibly also other metal species, be uniformly embedded in the mesoporous N-doped carbon shells to obtain robust hybrid hollow nanostructures for catalysts and possibly also other applications that require sufficient amounts of accessible metal species. Herein we demonstrate that the hollow nanospheres with mesoporous N-doped carbon shells of 10 nm and well-dispersed Fe_3O_4 nanoparticles show comparable ORR catalytic activity to that of commercial 20 wt% Pt/C catalyst, high electron transfer number (close to 4), better durability and higher tolerance to methanol crossover effect than the 20 wt% Pt/C catalyst.

2 Experimental

2.1 Materials

Tetraethyl orthosilicate (TEOS), ammonium hydroxide ($NH_3{\cdot}H_2O$, 28.0-30.0 % NH_3 basis), dopamine hydrochloride (DA), tris(hydroxymethyl) aminomethane (Tris) and $FeCl_3$ were purchased from Sigma-Aldrich (USA). Ethanol was supplied by Merck KGaA (Germany). All materials were used as received. Commercial 20 wt.% Pt/C catalyst was obtained from Aldrich (USA).

2.2 Synthesis of Fe-containing species- and N-doped carbon hollow nanospheres (Fe/N/C HNSs)

2.2.1 Synthesis of silica nanosphere template

SiO_2 nanosphere template (~100 nm) was prepared using the methods[32, 33] with slight modification. Firstly, 8 ml ammonia hydroxide was added into a solution containing 7.5 ml deionized water and 184.5 ml ethanol, and the mixed solution was stirred at 50 ^oC for 10 min. Then 8 ml of TEOS was added into the above-prepared mixture quickly under vigorous stirring and the reaction mixture was kept stirring under 50 ^oC for 2 h to yield uniform silica nanospheres. Finally, the product was centrifuged and washed using deionized water for three times.

2.2.2 Synthesis of Fe/N/C HNSs

The silica nanospheres covered with Fe^{3+}-PDA complexes (Fe^{3+}-PDA@SiO_2) were synthesized by polymerization of dopamine on SiO_2 templates in the Tris buffer (pH 8.5) in the presence of $FeCl_3$. In a typical procedure, 0.5 g SiO_2 was dispersed in 1000 mL deionized water under sonication, and 0.5 g dopamine and 0.213 g $FeCl_3$ were in turn added into the solution to form the complex (the solution color changed to dark green immediately). Then 1.21 g Tris was added into the solution after 10 min to initiate the polymerization of dopamine. The mixture was stirred at room temperature for 15 h, and the suspension was centrifuged, washed by deionized water for three times, and freeze-dried to obtain Fe^{3+}-PDA@SiO_2. For comparison purpose, different $FeCl_3$ amounts (0.141, 0.213, and 0.284 g) were used, *i.e.*, the molar ratios of dopamine to Fe^{3+} were 3/1, 2/1, and 1.5/1, respectively, at the fixed dopamine amount of 0.5 g, while the $FeCl_3$ amount of 0.213 g was used to prepare the Fe/N/C HNSs for catalyzing ORR unless otherwise specified. Carbonized samples (Fe/N/C@SiO_2) were obtained by annealing Fe^{3+}-PDA@SiO_2 in a tube furnace under Ar atmosphere at 650, 750, 800, and 850 °C, respectively, for 2 h. The hollow nanospheres (Fe/N/C HNSs) were obtained by removing SiO_2 template using 3 M KOH solution at 80 ^oC for 2 h, centrifuging, washing using deionized water for three times, and finally freeze-drying. The hollow nanospheres annealed at 650, 750, 800, and 850 °C are denoted as Fe/N/C HNSs-650, Fe/N/C HNSs-750, Fe/N/C HNSs-800, and Fe/N/C HNSs-850, respectively. In order to prepare the hollow nanospheres with thicker shells, the polymerization step was repeated twice to obtain a two-layer sample (Fe/N/C HNSs-750-2L) as a reference sample. A reference sample without Fe-containing species (N/C HNSs-750) was synthesized under the similar conditions to that for Fe/N/C HNSs-750 except in the absence of $FeCl_3$. Fe/N/C solid nanospheres-750 (Fe/N/C NSs-750) (*i.e.* without using SiO_2 template) was also prepared for comparison.

2.3 Characterization

The morphology and structures of the samples were studied using a field-emission scanning electron microscope (FESEM, JEOL-7600F) at an accelerating voltage of 5 kV and a transmission electron microscope (TEM, JEOL-2100F) operating at 200 kV. The Brunauer-Emmett-Teller (BET) specific surface area and Barrett-Joyner-Halenda (BJH) pore size of the samples were determined by nitrogen adsorption measurement at 77 K using a Micromeritics Tristar II-3020 nitrogen adsorption apparatus. X-ray photoelectron spectroscopy (XPS) measurements were conducted on a Kratos Analytical AXIS His spectrometer with a monochromatized Al Kα X-ray source (1486.6 eV photons). X-ray diffraction (XRD) patterns were recorded on a Bruker GADDS X-ray diffractometer.

2.4 Electrode preparation and electrochemical measurements

Prior to use, glassy carbon electrode (GCE, 5 mm in diameter, geometric area: 0.196 cm^2) was polished with 0.3 and 0.05 μm alumina powder slurry, respectively, and then ultrasonicated several times in ethanol and deionized water to get a mirror-like surface. Then, 5 mg as-prepared sample was dispersed in a mixture containing 784 μL deionized water, 196 μL ethanol and 20 μL Nafion solution (5%, Aldrich), and ultrasonicated for 30 min to form a homogeneous ink, followed by pipetting 10 μL of the ink onto a GCE substrate. The prepared electrodes were allowed to dry in air overnight, leading to an electrode loading of 0.255 mg cm^{-2}.

Electrochemical measurements for ORR were performed with a Pine biopotentiostat and a rotation speed controller (Pine Instrument Co.), using a typical three-electrode electrochemical cell including Ag/AgCl as the reference electrode, Pt as the counter electrode, and modified GCE as the working electrode, respectively. Cyclic voltammetry (CV) plots were collected in 0.1 M KOH solution at a scan rate of 10 mV s^{-1} from 0.2 to -1.0 V. Before each test, the electrolyte solution was saturated by bubbling argon or oxygen for at least 30 min. The polarization

curves for ORR (Linear sweep voltammograms) were obtained through the rotating disk electrode (RDE) technique in O_2-saturated 0.1 M KOH at a scan rate of 10 mV s^{-1} from 0.2 to -1.0 V under various rotation speeds (100, 400, 900, 1600, and 2500 rpm). 0.5 M H_2SO_4 was also used to study the ORR activity of the catalyst in the acidic medium. The ORR polarization curves are background corrected by subtracting the currents obtained under the same testing conditions in Ar-saturated electrolyte. All current densities were normalized to the geometric surface area of the electrode. Commercial Pt/C (20 wt %) with the same electrode loading (Pt/C) of 0.255 mg cm^{-2} was tested as reference under the same conditions.

3 Results and discussion

3.1 Preparation and characterization of Fe-containing species- and N-doped carbon hollow nanospheres (Fe/N/C HNSs)

The preparation route for Fe/N/C HNSs is schematically described in Figure 1. The morphologies and structures of the samples were characterized by FESEM and TEM, and the results are shown in Figure 2. The mean diameter of the silica nanosphere template is about 100 nm (Figures 2A and 2E). After the Fe^{3+}-mediated polymerization of dopamine, the silica nanospheres were covered with the Fe^{3+}-PDA complex coating due to PDA's chelating capability with metal ions. The effect of $FeCl_3$ amount on the structure and morphology of the Fe^{3+}-PDA@SiO_2 were studied, as shown in Figure S1, ESI†. When 0.213 g $FeCl_3$ is used, well separated Fe^{3+}-PDA@SiO_2 nanospheres with diameter of about 130 nm and uniform shell thickness of about 15 nm (Figure 2B, 2F and Figure S1B, S1E, ESI†) are obtained. However, when a smaller $FeCl_3$ amount of 0.141 g is used, aggregated Fe^{3+}-PDA@SiO_2 particles with uneven shell thickness of 15-25 nm (Figure S1A and S1D, ESI†) are obtained, in which several SiO_2 templates are coated by Fe^{3+}-PDA together, forming lager particles that are unfavorable for catalyzing ORR. When the $FeCl_3$ amount is increased to 0.284 g, many very small Fe^{3+}-PDA complex nanoparticles (about 15 nm) are formed and consequently the shell thickness on the SiO_2 template becomes very thin (about 5-10 nm), leading to broken HNSs after carbonization and removal of the template, as shown in Figure S1C and S1F, ESI†. Thus the $FeCl_3$ amount of 0.213 g was chosen to prepare the samples for catalyzing ORR unless otherwise specified. Annealing

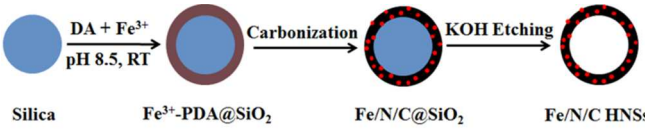

Figure 1. A schematic showing the route for preparation of the Fe/N/C HNSs.

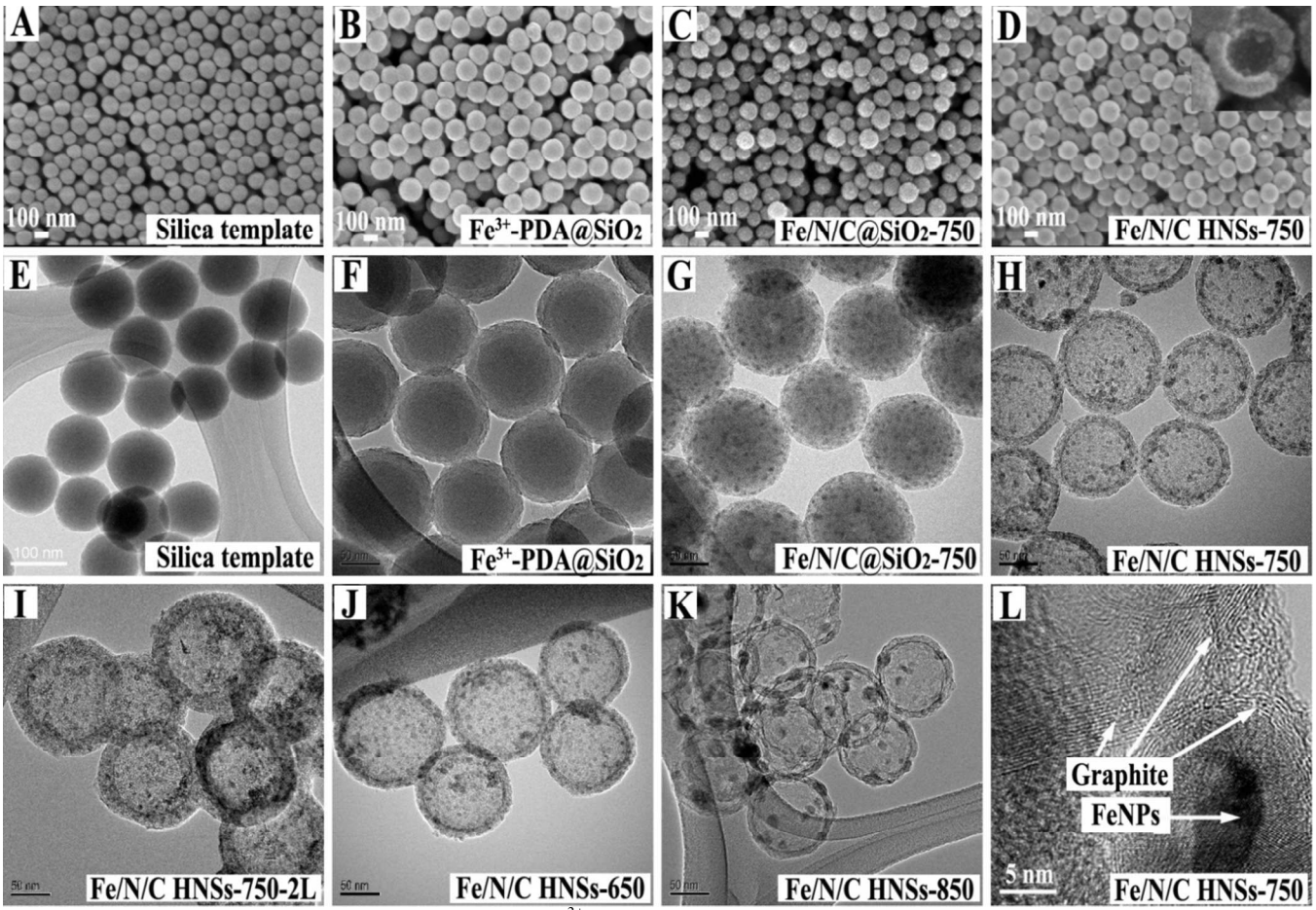

Figure 2. FESEM images of (A) silica template, (B) Fe^{3+}-PDA@SiO_2, (C) Fe/N/C@SiO_2-750, and (D) Fe/N/C HNSs-750. TEM images of (E) silica template, (F) Fe^{3+}-PDA@SiO_2, (G) Fe/N/C@SiO_2-750, (H) Fe/N/C HNSs-750, (I) Fe/N/C HNSs-750-2L, (J) Fe/N/C HNSs-650, (K) Fe/N/C HNSs-850, and (L) Fe/N/C HNSs-750 (HRTEM). The scale bar in (F-K) is 50 nm.

of Fe^{3+}-PDA@SiO_2 at 750 °C in Ar atmosphere resulted in carbonized PDA shell embedded with numerous well-dispersed Fe-containing nanoparticles (FeNPs) of about 9 nm and a reduction in shell thickness to about 10 nm (Figure 2C and 2G) due to the pyrolysis of PDA.[25] The uniform morphology of the coating before carbonization (Figure 2F) and the presence of homogeneously dispersed FeNPs in the carbon after carbonization (Figure 2G) verify the formation of the Fe^{3+}-PDA complex in the first step and FeNPs-embedded carbon after annealing. Finally, silica template was removed by etching using KOH solution at 80 °C, and hollow sphere morphology is remarkably uniform and clean (Figure 2D and 2H, the inset in 2D is the FESEM image at higher magnification). The mean diameter of the Fe/N/C HNSs is about 120 nm and shell thickness is about 10 nm. After polymerization of dopamine for two times, the shell thickness of Fe/N/C HNSs-750-2L approaches about 20 nm (Figure 2I). Figures 2J and 2K show TEM images of Fe/N/C HNSs-650 and Fe/N/C HNSs-850, respectively, from which we can see that the particle size of FeNPs increases with the annealing temperature (about 6, 9, and 14 nm for samples annealed at 650, 750, and 850 °C, respectively) and the particle size distribution of FeNPs in Fe/N/C HNSs-850 is less uniform and some FeNPs protrude from the carbon shell due to the aggregation of FeNPs at higher temperature of 850 °C. Moreover, the HRTEM (Figure 2L) of Fe/N/C HNSs-750 (Figure 2H) shows lattice-fringe of graphite structure and FeNPs, and well-defined graphitized carbon layers surrounding FeNPs are observed. Apart from the obvious advantage of high electrical conductivity, the graphitized carbon layers around FeNPs may promote the electrochemical activity and improve the stability of the ORR catalysts[18] because they can hinder the dissolution and agglomeration of FeNPs.[34, 35]

Nitrogen adsorption-desorption isotherms of Fe^{3+}-PDA@SiO_2, Fe/N/C@SiO_2-750, and Fe/N/C HNSs-750 are presented in Figure 3. Compared with Fe^{3+}-PDA@SiO_2 (22 m^2 g^{-1}) and Fe/N/C@SiO_2 (154 m^2 g^{-1}), Fe/N/C HNSs-750 shows much higher BET specific surface area (736 m^2 g^{-1}). It is observed that Fe/N/C HNSs-750 has a mesoporous structure with pore size distribution centered at around 2, 9, and 44 nm, respectively, as shown in the insets of Figure 3. The formation of the mesopores with dominant pore size of about 44 nm is due to the interspaces between the stacked nanospheres, as confirmed by FESEM and TEM studies (Figure 2D and 2H), while the smaller mesopores with sizes of about 2 and 9 nm may be formed by the diffusion and aggregation of Fe-containing species, the graphitization of carbon[25], and the release of volatiles during the annealing process. The markedly increased specific surface area of Fe/N/C HNSs-750 can be attributed to the abundant mesopores of the shell and hollow structure of Fe/N/C HNSs-750, which play a significant role in mass transfer in ORR.[24, 36]

XPS was used to analyze the elemental chemical states and contents in the sample, which would directly affect the electrochemical performance.[37-39] Figure 4A shows the survey spectra of Fe/N/C HNSs-750, revealing the presence of C, O and N (~2.7 at.%), as well as Fe (~10.6 at.%) in the catalyst. The overlapped high-resolution C1s peak were decomposed into four components (Figure 4B), which are arising from sp^2 hybridized C (284.5 eV), sp^3 C (285.4 eV), C-O and C=N (285.8 eV), and C-O-C and C-N (289.0 eV).[25] The high content of sp^2 C (about 57 at.% in total C species) would lead to high

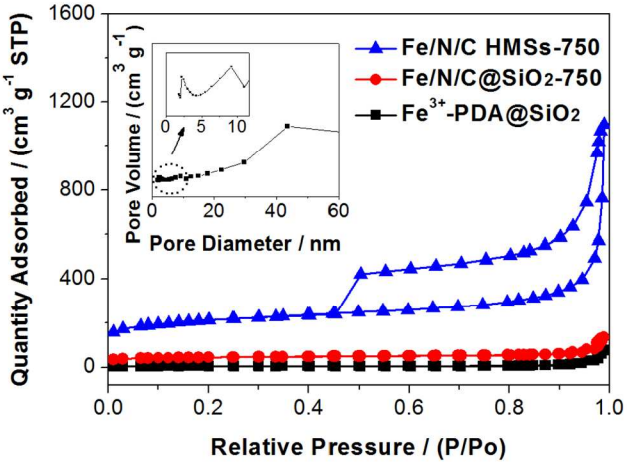

Figure 3. Nitrogen adsorption-desorption isotherms of Fe^{3+}-PDA@SiO_2, Fe/N/C@SiO_2-750, and Fe/N/C HNSs-750. Insets are BJH pore size distribution curves of Fe/N/C HNSs-750.

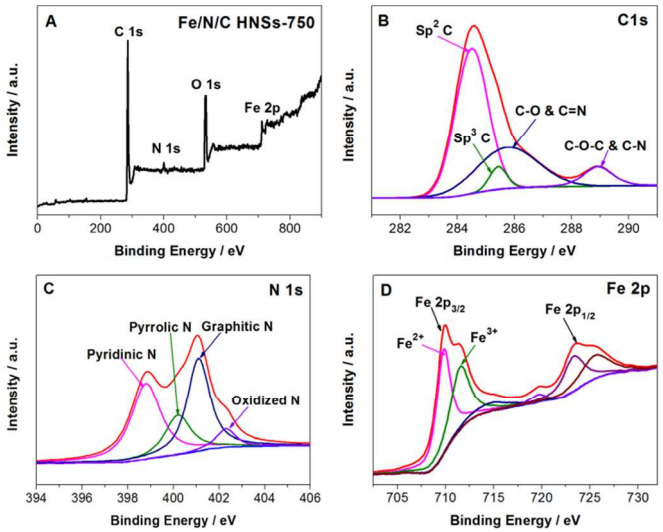

Figure 4. (A) XPS survey spectrum of Fe/N/C HNSs-750, and the corresponding high-resolution XPS spectra of (B) C 1s, (C) N 1s, and (D) Fe 2p.

electrical conductivity and hence high ORR activity. Nitrogen doping into carbon structure can strongly enhance the materials' electrochemical performance and play an important role in catalyzing ORR. Figure 4C shows the high-resolution N1s spectrum, which can be further deconvoluted into four different types of nitrogen species: pyridinic N (398.6 eV), pyrrolic N (400.2 eV), graphitic N (401.1 eV), and oxidized N (N-O) (402.3 eV).[12, 18, 40, 41] Pyridinic N bonds to two sp^2 carbon atoms at the edge of the carbon plane, graphitic N is bonded to three C atoms within a graphene plane, and the pyrrolic N is assigned to N atoms in a five-membered heterocyclic rings. Previous studies have indicated that the high electron affinity of N in the framework can induce positive charge density on an adjacent C atom, facilitating oxygen adsorption and subsequently weakening the bonding in the oxygen molecule.[3, 42, 43] Although N incorporation is an indispensable factor for the enhanced electrocatalytic activity in N-doped carbons, there is still a controversy on the roles of

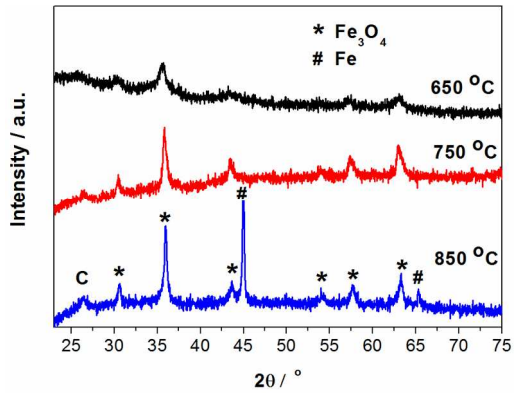

Figure 5. XRD patterns of Fe/N/C HNSs-650, -750, and -850.

various kinds of N heteroatoms in ORR.[44] Ruoff et al. concluded that graphitic-N could greatly increase the limiting current density while pyridinic-N could improve the onset potential for ORR and might convert the ORR reaction mechanism from a two-electron dominated process to a four-electron dominated one.[45] It was also reported that pyridinic N and graphitic N are of great significance in promoting the ORR activity.[46] In our case, the relative atomic percentages of pyridinic and graphitic N in Fe/N/C HNSs-750 were calculated to be 39.2% and 36.6% of the total N-species according to Figure 4C, indicating that they are predominant N species. This may explain the reason that the catalyst perform well for ORR, as described below. Noteworthily, ORR activity of metal/N/C catalysts possibly depends on how those atoms are incorporated into carbon rather than the quantity of doped nitrogen atoms in the catalysts.[18] Moreover, the high-resolution spectrum of Fe 2p of Fe/N/C HNSs-750 (Figure 4D) shows a distribution of Fe 2p into two species: Fe $2p_{3/2}$ at about 710 eV and Fe $2p_{1/2}$ at about 724 eV, which is consistent with previously reported spectra for Fe-containing species doped in carbon materials.[17, 47, 48] The co-existence of the two deconvoluted peaks at about 709.8 eV for Fe^{2+} and 711.5 eV for Fe^{3+} indicates that the Fe may exist in the form of Fe_3O_4 in the catalyst.[14, 49]

The XRD patterns (Figure 5) of Fe/N/C HNSs obtained by annealing at 650, 750, and 850 °C all exhibit the characteristic diffraction peaks at 2θ = 30.6, 35.9, 43.6, 54.0, 57.6, and 63.2°,[15] confirming the formation of Fe_3O_4 (JCPDS No. 65-3107). With the increase of pyrolysis temperature from 650 °C to 750 °C, the intensities of the characteristic peaks become stronger, indicating the increases of the crystallinity and particle size, which is consistent with TEM results (Figure 2). It should be pointed out that when the pyrolysis temperature is increased to 850 °C, the peaks at 44.9 and 65.3° appear, implying the formation of metallic Fe (JCPDS No. 87-0722) due to reduction of a part of Fe_3O_4 to Fe at elevated temperature.

3.2 Electrochemical activity of Fe/N/C HNS catalysts towards ORR

Cyclic voltammetry (CV) was employed to compare the electrocatalytic activity of N/C HNSs-750 (without Fe species) and Fe/N/C HNSs-750 for ORR in Ar- or O_2-saturated 0.1 M KOH solution (Figure 6A). It can be seen that both CV curves of N/C HNSs-750 and Fe/N/C HNSs-750 are essentially featureless in the Ar-saturated solution, whereas the two catalysts exhibit significant cathodic oxygen reduction peaks in O_2-saturated electrolyte. Compared with N/C HNSs-750, Fe/N/C HNSs-750 displays more pronounced ORR peak, more positive peak potential (-0.17 V *vs.* -0.22 V) and higher corresponding current density (-1.1 mA cm^{-2} *vs.* -0.7 mA cm^{-2}). The results strongly indicate that the coexistence of N and Fe_3O_4 dopants have significant effect on improving the ORR catalytic activity. Since the catalytic activity of pure oxidized iron species for ORR is low,[50] the high activity of Fe/N/C HNSs-750 could be attributed to a synergetic effect between the doped N and Fe_3O_4, *i.e.*, the active sites in the catalyst are the complex of doped N, Fe_3O_4 with C, which possesses much higher intrinsic activity for ORR than either N- or Fe_3O_4-doped active site.[8, 9, 14, 51]

The ORR activity of Fe/N/C HNSs-750 was also compared with that of the commercial 20 wt % Pt/C through polarization curves (Figure 6B) obtained by RDE technique in O_2-saturated 0.1 M KOH with scan rate of 10 mV s^{-1} at rotation rate of 1600 rpm. The half-wave potential is only slightly more negative than 20 wt% Pt/C (-0.22 V *vs.* -0.16 V), while the catalytic current density is even higher than that of the Pt/C below -0.53 V, suggesting that the catalyst is more kinetically facile toward ORR than Pt/C.[52] The possible reason is that the specific hollow structure with abundant mesopores and a large accessible surface area of Fe/N/C HNSs-750 leads to quick diffusion of reactants and products.

The effect of the pyrolysis temperature in the range of 650-850 °C on ORR activity of the Fe/N/C HNSs catalyst was also studied using RDE technique. The polarization curves in Figure 6C show that the Fe/N/C HNSs-750 exhibits higher ORR activity than Fe/N/C HNSs-650, Fe/N/C HNSs-800, and Fe/N/C HNSs-850 in terms of the onset and half-wave potentials, and current density over the whole potential range. The optimized annealing temperature of about 750 °C for Fe/N/C HNSs is slightly lower than 800 °C reported by Ai *et al.*[25] for preparing solid carbon sub-micrometer spheres possibly because the spheres prepared by different methods have different chemical compositions. When the annealing temperature increases from 650 °C to 750 °C, the sample possesses more sp^2 C, graphite-N and pyridinic-N,[25] which are in favor of better ORR performances. The further increase of the temperature to 800 and 850 °C, however, causes increases in particle size and less uniform particle size distribution due to the aggregation of FeNPs at elevated temperature, and the resultant particles contain both Fe_3O_4 and metallic Fe, as shown in the XRD pattern (Figure 5). Since the surface area of the Fe-containing nanoparticles is significantly reduced, ORR activity of the catalyst deteriorates.[18] The reduction of a part of Fe_3O_4 to Fe at 850 °C may also affect the ORR activity.

Figure 6D shows that compared with the samples without hollow core (Fe/N/C NSs-750 without template and Fe/N/C@SiO_2-750 without removing the template) and the sample with thicker shell (Fe/N/C HNSs-750-2L), Fe/N/C HNSs-750 shows more positive onset and half-wave potentials, and higher current density over the whole potential range. These imply that Fe/N/C HNSs-750 has better catalytic activity for ORR than the other samples, confirming that the morphology is one of the main factors for its excellent electrocatalytic activity. The hollow, porous and thin-shell morphology with high specific surface area allows more exposure of the active sites to the electrolyte, better utilization of the active materials, and more efficient transport and

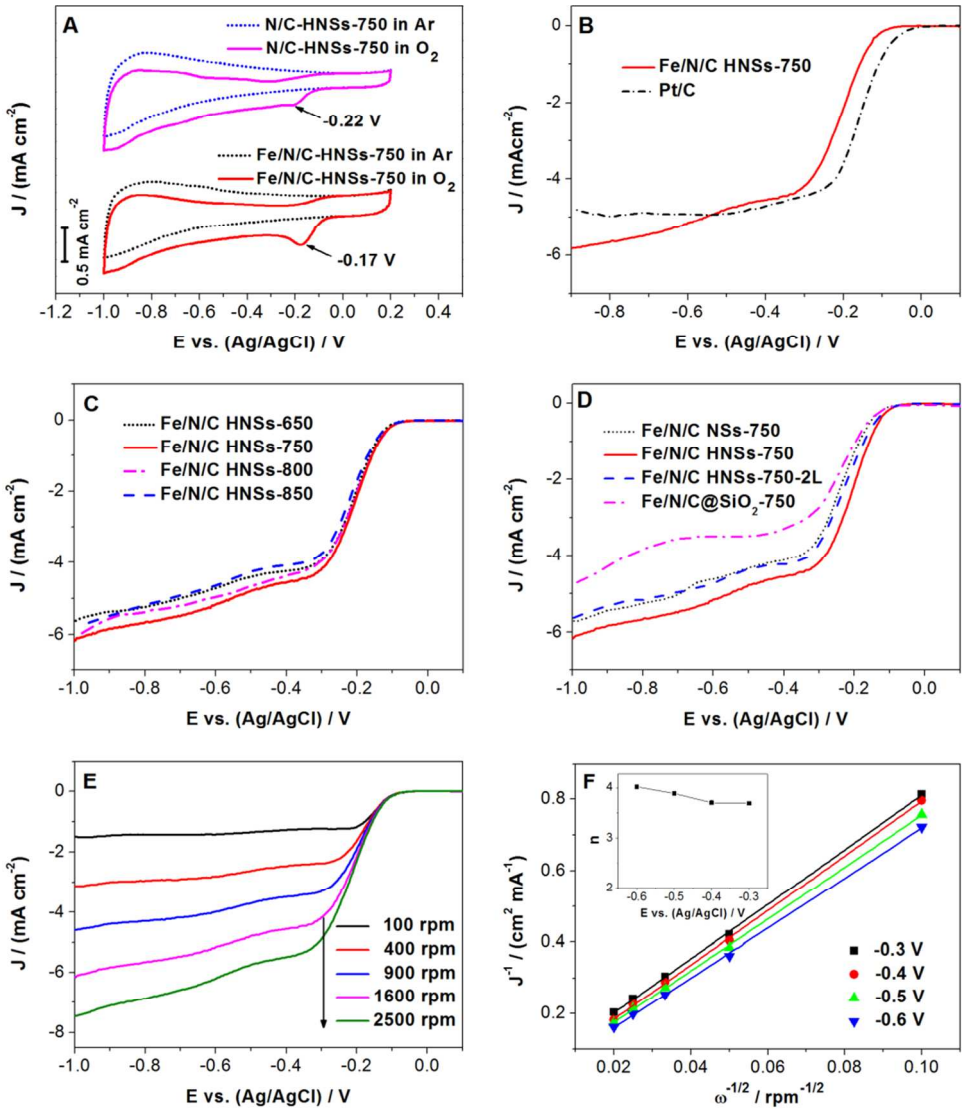

Figure 6. (A) CV curves of N/C HNSs-750 and Fe/N/C HNSs-750 in Ar- and O_2-saturated 0.1 M KOH solution (scan rate: 10 mV s^{-1}). (B) Polarization curves of Fe/N/C HNSs-750 and commercial Pt/C in O_2-saturated 0.1 M KOH solution, scan rate: 10 mV s^{-1}, rotation rate: 1600 rpm. (C) Polarization curves of Fe/N/C HNSs-650, 750, 800, and -850 in O_2-saturated 0.1 M KOH, scan rate: 10 mV s^{-1}, rotation rate: 1600 rpm. (D) Polarization curves of Fe/N/C NSs-750, Fe/N/C HNSs-750, Fe/N/C HNSs-750-2L, and Fe/N/C@SiO_2-750 in O_2-saturated 0.1 M KOH, scan rate: 10 mV s^{-1}, rotation rate: 1600 rpm. (E) Polarization curves of Fe/N/C HNSs-750 in O_2-saturated 0.1 M KOH at different rotation rates. (F) Koutecky-Levich plots of Fe/N/C HNSs-750 derived from polarization curves in (E) at different electrode potentials. Inset in (F) shows electron transfer number (n) at different potentials.

diffusion of electrolyte ions, electrons and O_2 during ORR because the active sites are expected to be easily accessible from both the inner and outer wall of the nanospheres.[39]

To further investigate the pathway and kinetic process of the ORR, polarization curves of the Fe/N/C HNSs-750 catalyst were recorded using RDE technique at different rotation rates (100, 400, 900, 1600 and 2500 rpm) in O_2-saturated solution with a scan rate of 10 mV/s (Figure 6E). The curves show an increase in the catalytic current density with rotation rate because of the enhanced diffusion of electrolytes.[3, 53, 54] According to the ORR polarization curves at various rotation rates, the corresponding Koutecky-Levich plots (Figure 6F) were obtained and exhibit good linearity with almost constant slope at electrode potentials ranging from -0.3 V to -0.6 V, indicating that the ORR process follows first-order kinetics with respect to the concentration of dissolved O_2.[3, 53] The overall electron transfer number (n) per oxygen molecule during the ORR can be calculated according to the Koutecky-Levich equation:[55]

$$\frac{1}{J}=\frac{1}{J_K}+\frac{1}{J_L}=\frac{1}{J_K}+\frac{1}{B\omega^{1/2}}$$

$$B=0.2nF(D_{O_2})^{2/3}\upsilon^{-1/6}C_{O_2}$$

where J is the measured current density at specific potential, J_k the kinetic current density, J_L the limiting diffusion current density and ω the RDE rotation rate. B could be determined

from the slope of the plots. n is the number of electrons transferred per molecule of O_2 reduced, F the Faraday constant (F = 96,485 C mol^{-1}), D_{O2} the diffusion coefficient of O_2 in 0.1 M KOH (1.9×10^{-5} cm^2 s^{-1}), υ the kinematic viscosity of 0.1 M KOH (0.01 cm^2 s^{-1}) and C_{O2} the bulk concentration of O_2 dissolved (1.2×10^{-6} mol cm^{-3}). There are two possible mechanism of ORR on different catalysts: the indirect two-electron pathway involving the formation of hydrogen peroxide as an intermediate and the direct four-electron pathway favorable in fuel cells because it offers higher kinetics of ORR.[39] In this case, the average n value is 3.8 (very close to 4) in the potential range of -0.6 V to -0.3 V (inset of Figure 6F); the high n value indicates good selectivity toward the four-electron pathway of ORR with H_2O as the main product during the cathodic reaction ($O_2 + 2H_2O + 4e^- \rightarrow 4OH^-$), similar to ORR catalyzed by a commercial Pt/C catalyst.[51] The high selectivity for the four-electron transfer pathway of Fe/N/C HNSs-750 can be attributed to the synergistic active sites created by doped N and Fe species.[8, 9, 14, 17, 51]

Fe/N/C HNSs-750 is also active for ORR in acidic solution, as confirmed by the CV and polarization curves of Fe/N/C HNSs-750 in 0.5 M H_2SO_4 (Figure S2, ESI†).

3.3 Durability and tolerance to methanol crossover effect

The electrocatalytic durability and tolerance to methanol crossover effect of ORR catalyst at the cathode are major concerns in practical application of fuel cells.[56] In Figure 7A, the current-time chronoamperometric response of Fe/N/C HNSs-750 at -0.26 V in O_2-saturated 0.1 M KOH solution at 1600 rpm exhibits a very good durability with a high relative current density of 87% of its initial current density after 20,000 s, whereas the Pt/C exhibits a more rapid attenuation with a current loss of 17%. Different from Pt/C, whose catalytic activity loss is due to the dissociation, migration and aggregation of Pt nanoparticles during the ORR,[19] Fe/N/C HNSs-750 possesses graphitized carbon shell on FeNPs, which suppresses the dissolution or agglomeration of FeNPs, and thus exhibits higher stability.

Fe/N/C HNSs-750 and commercial Pt/C catalysts were further compared by introducing fuel molecules (*e.g.*, methanol) into the electrolyte to examine their possible selectivity and crossover effects. As shown in Figure 7B, a strong current appears when O_2 is introduced at 1000 s due to ORR in the presence of the catalysts (Fe/N/C HNSs-750 or Pt/C). After adding 3.0 M methanol to O_2-saturated electrolyte at 2000 s, no change of the current track of ORR is observed for Fe/N/C HNSs-750. For Pt/C catalyst, however, a sharp change in the current density (converting from negative current for the ORR to positive current for the methanol oxidation reaction) appears when methanol is introduced, indicating susceptibility to methanol crossover of Pt/C. This result confirms that Fe/N/C HNSs-750 catalyst has much better tolerance to methanol crossover effect and higher fuel selectivity toward ORR than commercial Pt/C. This could greatly facilitate the development of commercial direct methanol fuel cells.

4. Conclusions

In summary, Fe/N/C HNSs can be readily prepared through polymerization of dopamine on SiO_2 nanospheres in the presence of $FeCl_3$, followed by carbonization and KOH etching

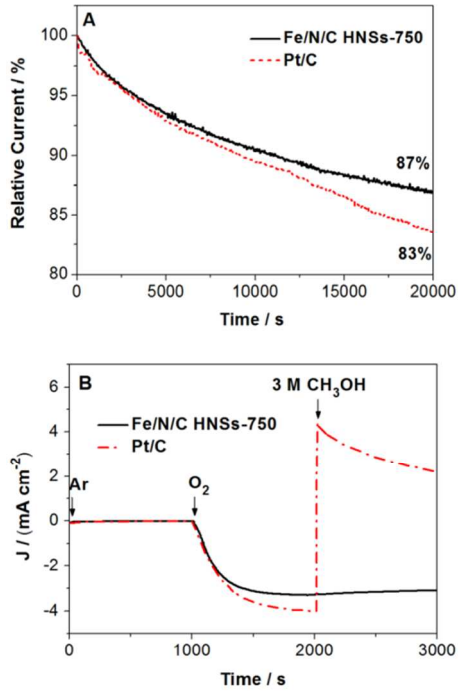

Figure 7. (A) Current-time chronoamperometric durability test (relative decrease of the current with time) of Fe/N/C HNSs-750 and Pt/C at -0.26 V in O_2-saturated 0.1 M KOH solution at a rotation rate of 1600 rpm. (B) Current-time response of Fe/N/C HNSs-750 and Pt/C at -0.26 V in Ar- (0-1000 s), O_2- (1000-2000 s), and O_2-saturated 0.1 M KOH solution with 3 M methanol (2000-3000 s) at a rotation rate of 1600 rpm.

of the SiO_2 templates. Compared with the commercial Pt/C catalyst, Fe/N/C HNSs-750 prepared by the one-pot doping process possesses comparably high catalytic activity, such as high onset and half-wave potentials, high current density, and high selectivity for four-electron transfer pathway, and superior electrocatalytic durability and methanol tolerance. The excellent catalytic properties of Fe/N/C HNSs-750 can be attributed to the following probable reasons: the high content of pyridinic nitrogen and graphitic nitrogen, the synergistic effect of doped N and Fe_3O_4 for ORR, graphitized carbon shell surrounding on Fe_3O_4 NPs, as well as unique porous hollow structure with ultrathin shell thickness and high surface area up to 736 m^2 g^{-1}. Therefore, the synthesized Fe/N/C HNSs-750 may serve as a promising nonprecious-metal alternative to commercial Pt/C catalyst for ORR. Furthermore, this one-pot doping strategy also has the potential for preparing other functional hybrid nanostructures by using different templates or introducing different metal species for catalyzing various reactions, as well as for other potential applications such as energy storage/conversion.

Notes and references

[a] *School of Materials Science and Engineering, Nanyang Technological University, 50 Nanyang Avenue, Singapore 639798. E-mail: asxhlu@ntu.edu.sg. Tel. No: +65-6790 4585. Fax No: +65-6790 9081*

[b] *Institute of Chemical and Engineering Sciences, A*STAR (Agency for Science, Technology and Research), 1 Pesek Road, Jurong Island, Singapore 627833, Singapore.*

† Electronic supplementary information (ESI) available: Figure S1 FESEM and TEM images of Fe^{3+}-PDA@SiO_2 prepared with different amounts of $FeCl_3$ and Figure S2 CV and Polarization curves of Fe/N/C HNSs-750 in 0.5 M H_2SO_4 solution. See DOI: 10.1039/x0xx00000x

1. P. Zhang, B. B. Xiao, X. L. Hou, Y. F. Zhu and Q. Jiang, *Sci Rep*, 2014, **4**, 3821.
2. W. Ding, Z. Wei, S. Chen, X. Qi, T. Yang, J. Hu, D. Wang, L.-J. Wan, S. F. Alvi and L. Li, *Angewandte Chemie-International Edition*, 2013, **52**, 11755-11759.
3. K. Gong, F. Du, Z. Xia, M. Durstock and L. Dai, *Science*, 2009, **323**, 760-764.
4. M. Lefevre, E. Proietti, F. Jaouen and J.-P. Dodelet, *Science*, 2009, **324**, 71-74.
5. G. Wu, K. L. More, C. M. Johnston and P. Zelenay, *Science*, 2011, **332**, 443-447.
6. J. Tian, A. Morozan, M. T. Sougrati, M. Lefevre, R. Chenitz, J.-P. Dodelet, D. Jones and F. Jaouen, *Angewandte Chemie-International Edition*, 2013, **52**, 6867-6870.
7. E. Proietti, F. Jaouen, M. Lefevre, N. Larouche, J. Tian, J. Herranz and J.-P. Dodelet, *Nature Communications*, 2011, **2**, 416.
8. S. Wang, E. Iyyamperumal, A. Roy, Y. Xue, D. Yu and L. Dai, *Angewandte Chemie-International Edition*, 2011, **50**, 11756-11760.
9. P. Chen, T.-Y. Xiao, Y.-H. Qian, S.-S. Li and S.-H. Yu, *Advanced Materials*, 2013, **25**, 3192-3196.
10. Y. Li, Y. Zhao, H. Cheng, Y. Hu, G. Shi, L. Dai and L. Qu, *Journal Of the American Chemical Society*, 2012, **134**, 15-18.
11. S. Wang, L. Zhang, Z. Xia, A. Roy, D. W. Chang, J.-B. Baek and L. Dai, *Angewandte Chemie-International Edition*, 2012, **51**, 4209-4212.
12. S. Chen, J. Bi, Y. Zhao, L. Yang, C. Zhang, Y. Ma, Q. Wu, X. Wang and Z. Hu, *Advanced Materials*, 2012, **24**, 5593-5597.
13. C. Xiao, X. Chu, Y. Yang, X. Li, X. Zhang and J. Chen, *Biosensors & Bioelectronics*, 2011, **26**, 2934-2939.
14. J. Liu, X. Sun, P. Song, Y. Zhang, W. Xing and W. Xu, *Advanced Materials*, 2013, **25**, 6879-6883.
15. H. Peng, Z. Mo, S. Liao, H. Liang, L. Yang, F. Luo, H. Song, Y. Zhong and B. Zhang, *Scientific Reports*, 2013, **3**, 1-7.
16. Z. Chen, D. Higgins, A. Yu, L. Zhang and J. Zhang, *Energy & Environmental Science*, 2011, **4**, 3167-3192.
17. B. J. Kim, D. U. Lee, J. Wu, D. Higgins, A. Yu and Z. Chen, *Journal Of Physical Chemistry C*, 2013, **117**, 26501-26508.
18. G. Wu and P. Zelenay, *Accounts Of Chemical Research*, 2013, **46**, 1878-1889.
19. J. Zhang, D. He, H. Su, X. Chen, M. Pan and S. Mu, *Journal Of Materials Chemistry A*, 2014, **2**, 1242-1246.
20. H.-W. Liang, W. Wei, Z.-S. Wu, X. Feng and K. Muellen, *Journal Of the American Chemical Society*, 2013, **135**, 16002-16005.
21. L. Zhang, J. Kim, E. Dy, S. Ban, K.-C. Tsay, H. Kawai, Z. Shi and J. Zhang, *Electrochimica Acta*, 2013, **108**, 480-485.
22. R. Liu, S. M. Mahurin, C. Li, R. R. Unocic, J. C. Idrobo, H. Gao, S. J. Pennycook and S. Dai, *Angewandte Chemie-International Edition*, 2011, **50**, 6799-6802.
23. H. Wang, X. Bo, A. Wang and L. Guo, *Electrochemistry Communications*, 2013, **36**, 75-79.
24. X.-H. Zhang, J.-D. Zhong, Y.-M. Yu, Y.-S. Zhang, B. Liu and J.-H. Chen, *Acta Physico-Chimica Sinica*, 2013, **29**, 1297-1304.
25. K. Ai, Y. Liu, C. Ruan, L. Lu and G. Lu, *Advanced Materials*, 2013, **25**, 998-1003.
26. J. Yan, L. Yang, M.-F. Lin, J. Ma, X. Lu and P. S. Lee, *Small*, 2013, **9**, 596-603.
27. H. Lee, S. M. Dellatore, W. M. Miller and P. B. Messersmith, *Science*, 2007, **318**, 426-430.
28. L. Yang, J. Kong, D. Zhou, J. M. Ang, S. L. Phua, W. A. Yee, H. Liu, Y. Huang and X. Lu, *Chemistry-a European Journal*, 2014, **20**, 7776-7783.
29. J. Kong, W. A. Yee, L. Yang, Y. Wei, S. L. Phua, H. G. Ong, J. M. Ang, X. Li and X. Lu, *Chemical Communications*, 2012, **48**, 10316-10318.
30. J. Kong, W. A. Yee, Y. Wei, L. Yang, J. M. Ang, S. L. Phua, S. Y. Wong, R. Zhou, Y. Dong, X. Li and X. Lu, *Nanoscale*, 2013, **5**, 2967-2973.
31. Y. Wei, J. Kong, L. Yang, L. Ke, H. R. Tan, H. Liu, Y. Huang, X. W. Sun, X. Lu and H. Du, *Journal Of Materials Chemistry A*, 2013, **1**, 5045-5052.
32. W. Stober, A. Fink and E. Bohn, *Journal Of Colloid And Interface Science*, 1968, **26**, 62-69.
33. G. H. Bogush, M. A. Tracy and C. F. Zukoski, *Journal Of Non-Crystalline Solids*, 1988, **104**, 95-106.
34. S. Yang, X. Feng, S. Ivanovici and K. Muellen, *Angewandte Chemie-International Edition*, 2010, **49**, 8408-8411.
35. Z.-S. Wu, S. Yang, Y. Sun, K. Parvez, X. Feng and K. Muellen, *Journal Of the American Chemical Society*, 2012, **134**, 9082-9085.
36. A. Stein, Z. Wang and M. A. Fierke, *Advanced Materials*, 2009, **21**, 265-293.
37. S. Maldonado and K. J. Stevenson, *Journal Of Physical Chemistry B*, 2004, **108**, 11375-11383.
38. Y. Tang, B. L. Allen, D. R. Kauffman and A. Star, *Journal Of the American Chemical Society*, 2009, **131**, 13200-13201.
39. J. Yan, H. Meng, F. Xie, X. Yuan, W. Yu, W. Lin, W. Ouyang and D. Yuan, *Journal Of Power Sources*, 2014, **245**, 772-778.
40. T. Sharifi, G. Hu, X. Jia and T. Wagberg, *Acs Nano*, 2012, **6**, 8904-8912.
41. Y. Ma, L. Sun, W. Huang, L. Zhang, J. Zhao, Q. Fan and W. Huang, *Journal Of Physical Chemistry C*, 2011, **115**, 24592-24597.
42. Z. Lin, M.-k. Song, Y. Ding, Y. Liu, M. Liu and C.-p. Wong, *Physical Chemistry Chemical Physics*, 2012, **14**, 3381-3387.
43. I.-Y. Jeon, D. Yu, S.-Y. Bae, H.-J. Choi, D. W. Chang, L. Dai and J.-B. Baek, *Chemistry Of Materials*, 2011, **23**, 3987-3992.
44. Y. Zheng, Y. Jiao, M. Jaroniec, Y. Jin and S. Z. Qiao, *Small*, 2012, **8**, 3550-3566.
45. L. Lai, J. R. Potts, D. Zhan, L. Wang, C. K. Poh, C. Tang, H. Gong, Z. Shen, J. Lin and R. S. Ruoff, *Energy & Environmental Science*, 2012, **5**, 7936-7942.
46. G. Liu, X. Li, P. Ganesan and B. N. Popov, *Applied Catalysis B-Environmental*, 2009, **93**, 156-165.
47. S. Li, Y. Hu, Q. Xu, J. Sun, B. Hou and Y. Zhang, *Journal Of Power Sources*, 2012, **213**, 265-269.
48. K. Kamiya, K. Hashimoto and S. Nakanishi, *Chemical Communications*, 2012, **48**, 10213-10215.
49. L. Wang, J. Yin, L. Zhao, C. Tian, P. Yu, J. Wang and H. Fu, *Chemical Communications*, 2013, **49**, 3022-3024.
50. G. Wu, C. M. Johnston, N. H. Mack, K. Artyushkova, M. Ferrandon, M. Nelson, J. S. Lezama-Pacheco, S. D. Conradson, K. L. More, D. J. Myers and P. Zelenay, *Journal Of Materials Chemistry*, 2011, **21**, 11392-11405.
51. Y. Liang, Y. Li, H. Wang, J. Zhou, J. Wang, T. Regier and H. Dai, *Nature Materials*, 2011, **10**, 780-786.
52. Z. Jiang, Z.-j. Jiang, X. Tian and W. Chen, *Journal Of Materials Chemistry A*, 2014, **2**, 441-450.
53. R. Liu, D. Wu, X. Feng and K. Muellen, *Angewandte Chemie-International Edition*, 2010, **49**, 2565-2569.
54. X. Zhong, H. Yu, G. Zhuang, Q. Li, X. Wang, Y. Zhu, L. Liu, X. Li, M. Dong and J.-g. Wang, *Journal Of Materials Chemistry A*, 2014, **2**, 897-901.
55. D. Yu, Q. Zhang and L. Dai, *Journal Of the American Chemical Society*, 2010, **132**, 15127-15129.
56. S.-H. Liu, J.-R. Wu, C.-J. Pan and B.-J. Hwang, *Journal Of Power Sources*, 2014, **250**, 279-285.

